Nano Research

Open Access

Research Article

S/Ge dual gradient spontaneous construction for improved CZTSSe solar cells

Yingbi Zhao[1,2,3,4], Qiang Li[1,2,3,4], Wencong Tian[1,2,3,4], Zhixiao He[1,2,3,4], Shaofan Gao[1,2,3,4], Jingling Liu[1,2,3,4] ✉, Xinsheng Liu[1,2,3,4], Ke Cheng[1,2,3,4] ✉, and Zu-liang Du[1,2,3,4] ✉

[1] *Key Laboratory for Special Functional Materials of Ministry of Education, Henan University, Kaifeng 475004, China*
[2] *National & Local Joint Engineering Research Center for High-efficiency Display and Lighting Technology, Henan University, Kaifeng 475004, China*
[3] *School of Materials Science and Engineering, Henan University, Kaifeng 475004, China*
[4] *Collaborative Innovation Center of Nano Functional Materials and Applications, Henan University, Kaifeng 475004, China*

Cite this article: *Nano Research*, **2026**, *19*, 94908520. https://doi.org/10.26599/NR.2026.94908520

ABSTRACT: A key reason for $Cu_2ZnSn(S,Se)_4$ (CZTSSe, 15.8%) solar cells lagging far behind $Cu(In,Ga)Se_2$ (CIGS, 23.6%) in efficiency is its inability to autonomously form a dual-gradient bandgap via Ga gradient, critical for the simultaneous efficient light absorption and directed carrier transport. Herein, this study proposes a novel strategy for the spontaneous construction of dual gradients CZTSSe with a S-rich front interface and a Ge-rich back interface based on SnS-GeSe co-sulfoselenization. SnS releases S vapor and Sn_2Se_3 intermediate phase during selenization, synchronously compensating for Sn volatilization loss and forming a S-rich surface layer, leading to a synergistic composition stability and interface defect passivation. Meanwhile, GeSe, by virtue of its eutectic property, promotes the migration and enrichment of Ge toward the back interface for an efficient back surface field and suppresses defects. The S-rich front widens the surface bandgap to improve open-circuit voltage (V_{OC}), and the Ge-rich back elevates the back conduction band minimum (CBM) and suppresses the Sn-related defect to facilitate carrier transport. As a positive result, the optimized devices achieve a 26% enhancement in photovoltaic efficiency, offering a new insight for the development of high-efficiency kesterite-based solar cells.

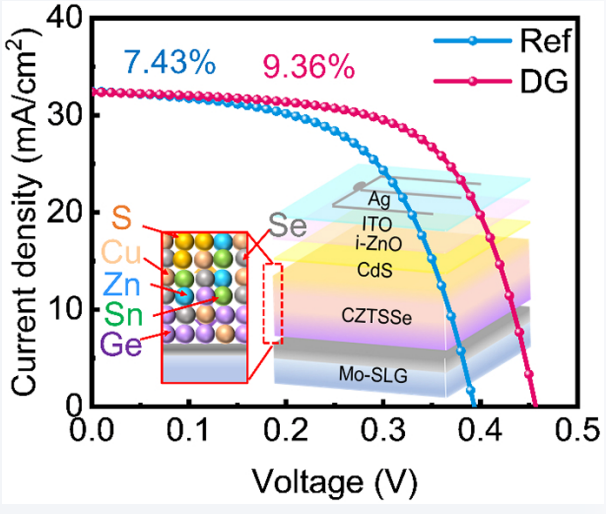

KEYWORDS: $Cu_2ZnSn(S,Se)_4$ (CZTSSe), dual-gradient band structure, sulfoselenization, defect passivation

1 Introduction

$Cu_2ZnSn(S,Se)_4$ (CZTSSe) thin-film solar cells have emerged as a promising alternative to traditional $Cu(In,Ga)Se_2$ (CIGS) because of their direct and tunable bandgap (1.0–1.5 eV), high absorption coefficient (10^4 cm^{-1}), and environmental friendliness [1, 2]. However, their highest certified power conversion efficiency (PCE) remains only 15.8% [3], still significantly lagging CIGS cells (23.6%) [4]. This bottleneck primarily stems from a substantial open-circuit voltage (V_{OC}) deficit, which originates from two key factors: (1) severe non-radiative recombination caused by abundant interface defects and bulk deep-level defects/clusters, and (2) interfacial recombination induced by band mismatch at the heterojunction [5–8].

Notably, in high-efficiency CIGS cells, the dual-gradient bandgap structure achieved through gradient distribution of Ga has been established as a mature pathway to overcome efficiency limitations [9]. This configuration enables efficient broadband light absorption and facilitates directional carrier transport, thereby simultaneously enhancing V_{OC} and short-circuit current density (J_{SC}). However, directly migrating this strategy to the CZTSSe system is challenging due to two fundamental factors. On one hand, the similar diffusion rates of elements in CZTSSe hinder the spontaneous formation of a

Received: December 9, 2025; **Revised:** January 29, 2026
Accepted: February 1, 2026

✉Address correspondence to Jingling Liu, jingling@henu.edu.cn; Ke Cheng, ck@henu.edu.cn; Zu-liang Du, zld@henu.edu.cn

stable compositional gradient via conventional processes [10]. On the other hand, the high volatility of Sn at elevated temperatures leads to compositional deviation [11–13], which severely disrupts the continuity of the band structure.

To address these challenges, current research focuses primarily on two strategies. Firstly, elemental gradient doping (e.g., K_2S interface engineering, Cd gradient alloying, and Ag/Ge doping) aims to construct bandgap gradients through localized compositional modulation [14–17]. Secondly, precursor process optimization (e.g., multi-layer spin-coating or multi-step annealing) attempts to control element distribution via precise precursor manipulation [18, 19]. Nevertheless, these approaches not only face challenges related to process complexity but also predominantly focus on unilateral optimization, struggling to synergistically address bulk/interface defect suppression and graded bandgap construction within a single, simplified process, being highly motivated in this work.

In the fabrication process of CZTSSe films, existing process exploration indicates that SnS_x or $SnSe_x$ are commonly used as a selenization additive to compensate for the Sn loss and assist grain growth [20, 21]. However, this predominantly focuses on the compensatory role of cations (Sn) while overlooking the potential of anions (S/Se) gradient regulation. In fact, the differences in the conduction and valence band energies between S and Se theoretically allow for the formation of a favorable bandgap gradient, optimizing interfacial alignment with the CdS buffer layer [22]. Additionally, research has shown that $GeSe_x$ not only acts as a selenization aid promoting CZTSSe grain growth but also, via Ge doping or diffusion, suppresses defects/clusters, such as Cu_{Sn} and [$2Cu_{Zn}$ + Sn_{Zn}], thereby reducing interfacial non-radiative recombination [23]. Furthermore, our preliminary studies utilizing a GeSe-Se co-selenization process demonstrated the spontaneous formation of a back-surface Ge gradient, highlighting the feasibility of such gradient regulation and defect passivation synergistic modulation [24, 25].

On this basis, we innovatively propose a SnS-GeSe co-sulfoselenization process, which exploits the distinct thermodynamic behaviors of SnS and GeSe (melting/boiling points, vapor pressures, and the low-eutectic characteristics of the Ge–Se system) to spontaneously construct a dual-graded CZTSSe with an S-rich front interface and a Ge-rich back interface. The key advantages of this process are reflected in three aspects: (1) A stable gradient can be formed spontaneously by virtue of the intrinsic properties of the materials, without the need for sophisticated temperature-control techniques; (2) efficient synergistic utilization of cations and anions is realized, where SnS decomposition compensates for Sn loss while the released S accumulates at the front surface of the absorber, to passivating surface/interface defects [20]; and (3) benefiting from the low-eutectic nature of Ge–Se [26], Ge is driven to diffuse toward the back interface to construct a Ge-rich back gradient, while Ge incorporation further suppresses Sn-related defects/clusters, thereby achieving both gradient formation and defect suppression. As a result, the PCE of CZTSSe solar cells is enhanced from 7.43% to 9.36%. This improvement is attributed to the synergistic effects of front-interface defect passivation, band-structure optimization, and reinforced carrier transport kinetics, providing a new pathway for the development of low-cost, high-efficiency, and stable kesterite solar cells.

2 Results and discussion

2.1 Construction and validation of the dual gradient

Figure 1(a) illustrates the fabrication process of the S/Ge dual-gradient CZTSSe absorber layer. (1) Using a direct current (DC) magnetron sputtering system, Zn, Sn, and Cu metal layers are sequentially deposited onto a molybdenum-coated soda-lime glass (Mo-SLG) substrate to form a stacked precursor layer. (2) The precursor layer and powders of S, Se, SnS, and GeSe are placed in separate zones within a rapid thermal processing (RTP) furnace for a one-step co-sulfoselenization reaction. This ultimately forms a dual-gradient CZTSSe absorber layer with an S-rich front interface and a Ge-rich back interface. Detailed experimental procedures are provided in the supporting information. To optimize the sulfoselenization process, we investigated the effects of SnS and GeSe powder loading on film quality and device performance (Figs.

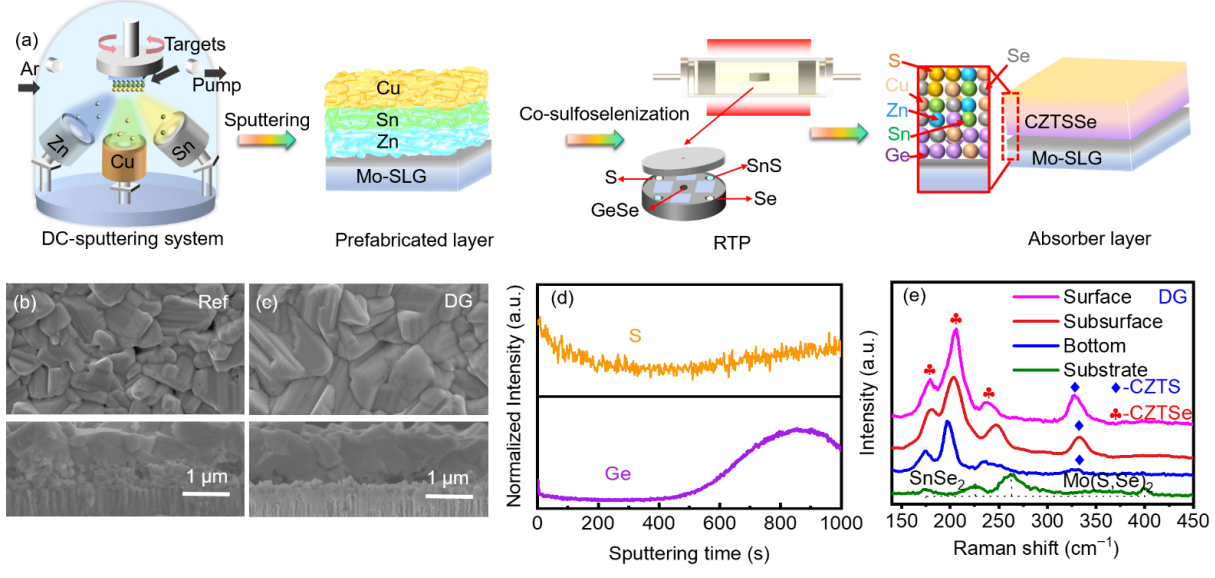

Figure 1 (a) Preparation process of the dual-gradient CZTSSe absorber. ((b) and (c)) Top-view and cross-section SEM images of Ref and DG. (d) Normalized SIMS elemental spectra of S and Ge in DG. (e) Raman spectra of the DG sample.

S1 and S2 and Table S1 in the Electronic Supplementary Material (ESM)). Optimal process conditions were determined as Sn-20 and Ge-20, with detailed performance parameters shown in Fig. S3 and Tables S2 and S3 in the ESM. Subsequent dual-gradient studies were conducted under these optimal conditions, without any additions labeled as Reference (Ref) and dual-gradient samples as Dual Gradient (DG).

Figures 1(b) and 1(c) show the scanning electron microscopy (SEM) images of the Ref and DG samples. In contrast to the Ref sample, the DG sample exhibits more uniform and densely packed grains, improved crystallinity, a significantly thinner fine-grain layer, reduced void density, and stronger interfacial adhesion to the Mo-SLG substrate, factors that collectively contribute to a notable enhancement in the overall quality of the absorber film. Figure 1(d) and Fig. S4 in the ESM illustrate the time-of-flight secondary-ion mass spectrometry (SIMS) depth profiling of the DG absorber layer, revealing that the S signal intensity decreases progressively with increasing sputtering time (corresponding to greater depth within the film), reflecting a clear S enrichment at the front surface. Conversely, the Ge signal exhibits a continuous increase with depth, confirming the formation of a Ge-rich region near the back interface (substrate side). This distinct dual-gradient distribution is structurally analogous to the bidirectional Ga gradient employed in high-efficiency CIGS solar cells [27], which facilitates simultaneous improvements in V_{OC} and J_{SC}, suppresses carrier recombination and broadens the spectral response range.

Further validation was performed via Raman spectroscopy with depth-resolved analysis (using a 532 nm laser with an approximate penetration depth of 50 nm, corresponding to the surface region; a 785 nm laser with an approximate penetration depth of 150 nm, corresponding to the subsurface region; and bottom-layer spectra obtained after etching with aqua regia (a mixture of nitric acid (HNO_3) and hydrochloric acid (HCl))) [28]. As shown in Fig. 1(e), the intensity of the 327 cm^{-1} Raman peak, corresponding to the A_1 vibrational mode of Cu_2ZnSnS_4 (CZTS) [29], progressively decreases from the surface toward the bottom in the DG sample, which is consistent with the secondary ion mass spectrometry (SIMS) results. In contrast, the Ref sample exhibits a slight increase in A_1 peak intensity from top to bottom (Fig. S5(a) in the ESM). This trend correlates with the reverse S gradient observed in the Ref sample (Fig. S5(b) in the ESM), demonstrating that the introduction of SnS effectively promotes sulfur enrichment at the front surface.

Further evidence for the dual-gradient distribution was obtained through ultraviolet–visible–near infrared ray (UV–vis–NIR) spectroscopy and ultraviolet photoelectron spectroscopy (UPS). Figure 2 systematically compares the optical properties and band structures at the surface and bottom regions of the Ref and DG samples. Tauc plots constructed from the absorption spectra reveal that the DG sample exhibits enlarged bandgaps (E_g) at both the surface (1.02 eV) and the bottom (1.05 eV), compared to the Ref sample (0.97 eV at the surface, 0.99 eV at the bottom). This bandgap widening is directly attributable to the established S/Ge compositional gradient. UPS measurements further elucidate the detailed electronic structure, with corresponding band alignment calculations provided in Note S1 in the ESM. At the surface, the Fermi level (E_F) of DG exhibits a slightly larger band gap difference with the valence band maximum (VBM) (0.39 eV) than Ref (0.37 eV), and a slightly larger difference with the conduction band minimum (CBM) (0.63 eV) than Ref (0.60 eV). This indicates slight downward and upward shifts of the surface VBM and CBM, respectively, in the DG sample. At the bottom, the band gap between the E_F and CBM (0.65 eV) in DG is significantly larger than that in Ref (0.56 eV), indicating a more pronounced upward shift of the CBM. The band diagram in Fig. 2(f) schematically depicts the graded band alignment in the DG sample. This band structure modulation stems from the composition characteristics of the band structure of CZTSSe. The VBM of CZTSSe is primarily

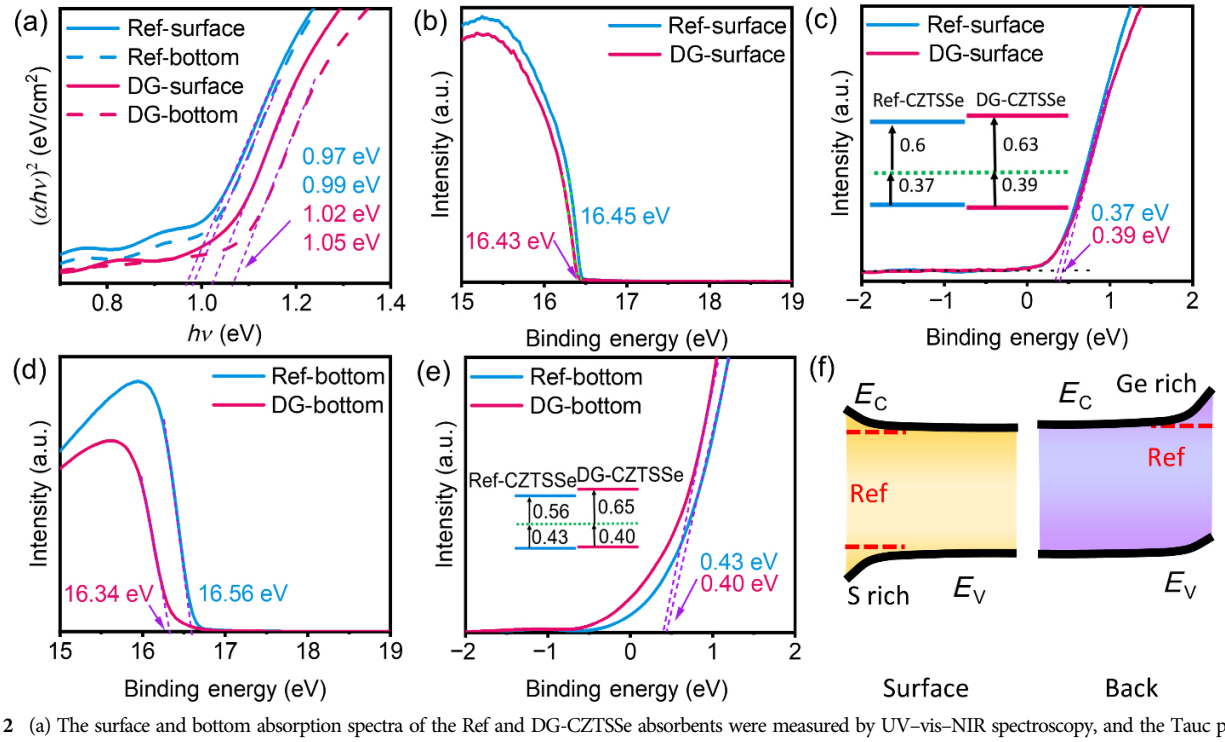

Figure 2 (a) The surface and bottom absorption spectra of the Ref and DG-CZTSSe absorbents were measured by UV–vis–NIR spectroscopy, and the Tauc plot was fitted. ((b)–(e)) UPS measurements of sample surfaces and bottoms. (f) Schematic of band bending at the front and back interfaces of DG.

constituted by the anti-bonding interaction between Cu 3d and S/Se 3p orbitals, whereas the CBM originates from the hybridization of Sn 5s with S/Se 3s and 3p orbitals [30]. At the front surface, the enriched S atoms, characterized by higher electronegativity, strengthen the anti-bonding interaction with Cu 3d orbitals. Their smaller atomic radius shortens chemical bonds and enhances orbital hybridization, collectively resulting in a downward shift of the VBM and an upward shift of the CBM, thereby widening the surface bandgap. At the back interface, Ge^{4+} enrichment driven by the smaller ionic radius of Ge^{4+} compared to Sn^{4+} reduces the Sn 5s contribution to the CBM and introduces higher-energy Ge 4s orbitals into the hybridization process [31], thereby inducing a further upward shift of the CBM. In summary, surface S enrichment enhances V_{OC} through bandgap widening, while back-surface Ge enrichment facilitates carrier transport by elevating the CBM, collectively enabling optimized band alignment and gradient formation.

2.2 Formation mechanism of dual gradient

The formation of the dual-gradient structure, comprising an S-rich front surface and a Ge-rich back interface, originates from the synergistic effects of saturated vapor pressure differences, competitive reaction kinetics, and phase evolution. To elucidate the behavior of individual substances during the process, we first evaluated the temperature-dependent saturated vapor pressures of Se, S, SnS, and GeSe, as summarized in Fig. 3(a) (Note S2 in the ESM for calculation details). The results indicate that S exhibits a higher saturated vapor pressure than Se, rendering it more volatile during reaction, whereas SnS shows the lowest vapor pressure, suggesting that significant evaporation occurs predominantly in the later reaction stages. To further clarify the underlying reaction mechanism, we subjected SnS, GeSe, and SnS-GeSe powder mixtures to sulfoselenization and analyzed the residues using X-ray diffraction (XRD) and Raman spectroscopy (Figs. 3(b) and 3(c) and Fig. S6 in the ESM). Residues are represented by RGeSe and RSnS, respectively. The analysis shows that the characteristic diffraction peaks of SnS and GeSe disappear after sulfoselenization, with their positions replaced by those of $SnSe_2$ and $GeSe_2$ [32], confirming that SnS and GeSe participate in the following chemical reactions during sulfoselenization

$$2SnS + 4Se \rightarrow 2SnSe_2 + S_2 \quad (1)$$

$$2SnS + 3Se \rightarrow Sn_2Se_3 + S_2 \quad (2)$$

$$SnSe_2 \rightarrow SnSe + Se \quad (3)$$

$$GeSe + Se \rightarrow GeSe_2 \quad (4)$$

During the initial reaction stage, sulfur atoms possess a small atomic radius, high reactivity, and large saturated vapor pressure. These properties enable S_2 vapor to readily diffuse toward the surface of the metallic precursor layer and facilitate rapid formation of metal sulfides [33]. In contrast, selenium exhibits lower vapor pressure, a larger atomic radius, and relatively weaker reactivity, resulting in delayed selenization and an initial accumulation of sulfur near the substrate back interface. As the reaction proceeds, sufficient Se fully selenizes the precursor layer and partially converts it into the $Cu_2ZnSnSe_4$ (CZTSe) phase. At this stage, the lower saturated vapor pressure of SnS causes its delayed volatilization. The subsequently released SnS vapor reacts with Se vapor, continuously generating S_2 that replenishes the front surface sulfur source (Eqs. (1) and (2)), thereby enhancing S accumulation at the front interface. Thermodynamic data (Tables S4 and S5 in the ESM) further indicate that the formation enthalpy (ΔH) of sulfides is more negative than that of selenides, which thermodynamically promotes the conversion of surface selenides into sulfides and further enhances front surface S enrichment. In addition, Sn compensates for high temperature volatilization losses through gaseous species, such as Sn_2Se_3 or SnSe (Eqs. (2) and (3)), thereby contributing to stabilizing the stoichiometry of the absorber layer [34].

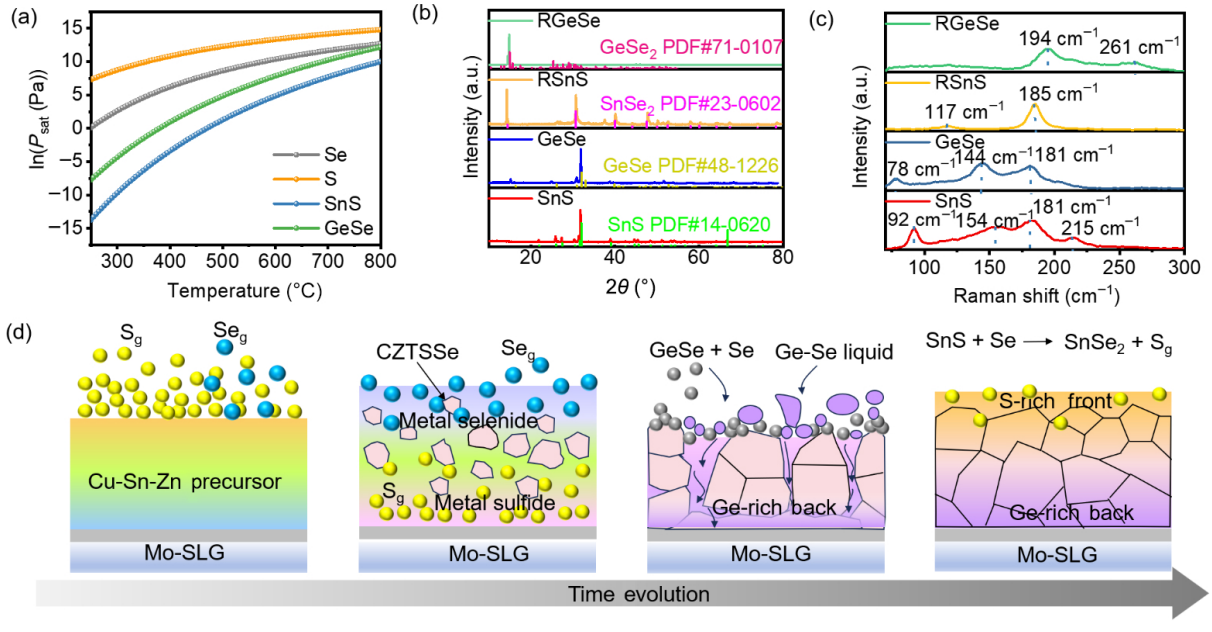

Figure 3 (a) Relationship between saturated vapor pressure and temperature for Se, S, SnS, and GeSe materials. ((b) and (c)) XRD and Raman characterization of SnS and GeSe powders before and after sulfur-selenium treatment. (d) Schematic illustration of the formation mechanism of the absorption layer under DG conditions.

Regarding the Ge enrichment at the back interface, although GeSe exhibits a higher saturated vapor pressure than SnS, the resulting $GeSe_2$ from its reaction with Se readily forms a Ge-Se liquid eutectic phase. This liquid medium enhances the migration of Ge atoms toward the bottom of the absorber layer, where they solidify and accumulate (as detailed in our previous paper [24, 25]). The corresponding mechanism is schematically illustrated in Fig. 3(d). It is noteworthy that this approach realizes dual-gradient formation via a single heat-treatment step, thereby streamlining the fabrication process and overcoming the challenge of spontaneous dual-gradient construction in CZTSSe absorbers.

2.3 Fundamental characterization

Through multiple techniques, including XRD, Raman spectroscopy, and X-ray photoelectron spectroscopy (XPS), the differences between Ref and DG-CZTSSe samples in crystal structure, defect properties, and elemental valence states were systematically compared. The XRD patterns in Fig. 4(a) show that both Ref and DG samples exhibit characteristic diffraction peaks of kesterite CZTSSe (e.g., (011), (112), (220), and (312)), indicating that the dual gradient structure does not change the fundamental crystal phase. However, the DG sample shows enhanced peak intensity and narrowed full width at half maximum (FWHM), reflecting improved crystallinity [35], which aligns with the SEM results. Additionally, the (112) peak of the DG sample exhibits a slightly higher diffraction angle than the Ref sample. In accordance with Bragg's law, this shift signifies a reduced lattice constant for the DG sample, which is attributed to lattice contraction arising from the substitution of larger Sn^{4+} and Se^{2-} ions by smaller Ge^{4+} and S^{2-} ions, thereby validating the effective incorporation of Ge/S in the absorption layer.

Figure 4(b) shows the normalized Raman spectra under 532 nm laser excitation. The DG sample exhibits the weakest characteristic B-mode peak intensity at approximately 173 cm^{-1}, suggesting the higher concentration of beneficial [V_{Cu} + Zn_{Cu}] defect clusters according to prior reports [36–38]. Simultaneously, the characteristic peak intensity of the E mode at ~ 235 cm^{-1} is reduced, indicating a decrease in the density of [$2Cu_{Zn}$ + Sn_{Zn}] harmful defect clusters, which effectively suppresses tail states and non-radiative recombination. Furthermore, the Ref sample exhibits a broadened selenium-like peak at ~ 196 cm^{-1} due to phonon confinement effects arising from its poor crystal quality and high defect density [39]. The rightward shift of the main peak at ~ 196 cm^{-1} in the inset, consistent with XRD results, further confirms the successful introduction of Ge^{4+} and its induced lattice contraction.

The XPS data in Figs. 4(c)–4(f) and Fig. S7 in the ESM systematically reveal the optimizing effect of the S/Ge dual gradient on the valence states of elements in the CZTSSe absorption layer. The Sn 3d spectra show that the 8.4 eV splitting between the $3d_{5/2}$ (486.5 eV) and $3d_{3/2}$ (494.9 eV) peaks corresponds to the Sn^{4+} valence state, while the shoulder peak at 497–498 eV, attributed to Zn Auger peaks or Zn-based secondary phases/defects [40], is significantly weakened in the DG sample. Further fitting of the Sn $3d_{5/2}$ peak reveals that a reduction in the Sn^{2+} content from 56% (Ref) to 9% (DG), indicating effective suppression of Sn-related defects and secondary phases [41]. Concurrently, the Ge $3d_{5/2}$ (25.70 eV) and $3d_{3/2}$ (26.70 eV) peaks in Fig. 4(f), characteristic of Ge^{4+} [42], confirm the successful incorporation of Ge into the lattice. Figure S7 in the ESM confirms that Cu exists primarily as Cu^{+}, Zn as Zn^{2+}, and both Se and S as −2 in Ref and DG samples. However, the DG sample exhibits greater purity, demonstrating effective optimization of elemental distribution and suppression of defects through the dual-gradient strategy.

Figure 5 summarizes the surface morphology and local electronic structure of the Ref and DG absorber layers using atomic force microscopy (AFM) and Kelvin probe force microscopy (KPFM). The DG sample exhibits a reduced surface roughness (102 nm)

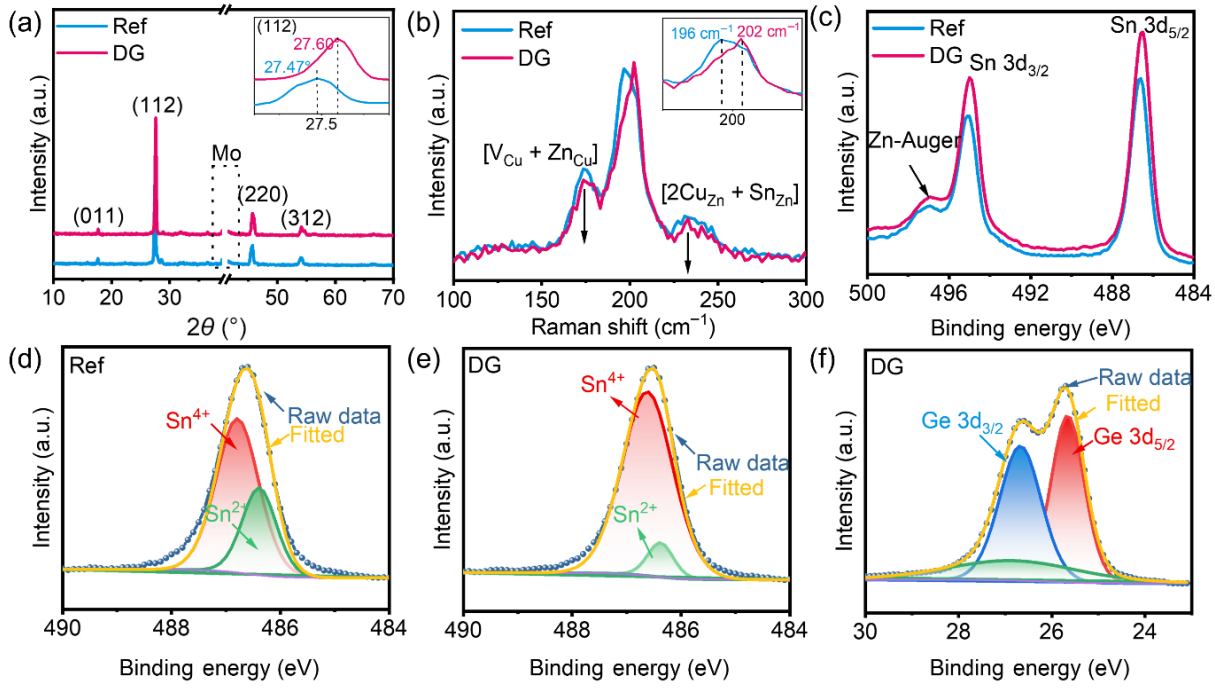

Figure 4 (a) XRD patterns of Ref and DG, with the inset showing an enlarged view of the main (112) peak. (b) Normalized Raman spectra of the CZTSSe absorber layer, with the inset showing a magnified view of the main peak at 198 cm^{-1}. (c) Sn 3d peaks of Ref and DG. ((d) and (e)) XPS spectra of the Sn 3d region for Ref and DG. (f) XPS spectrum of the Ge 3d region.

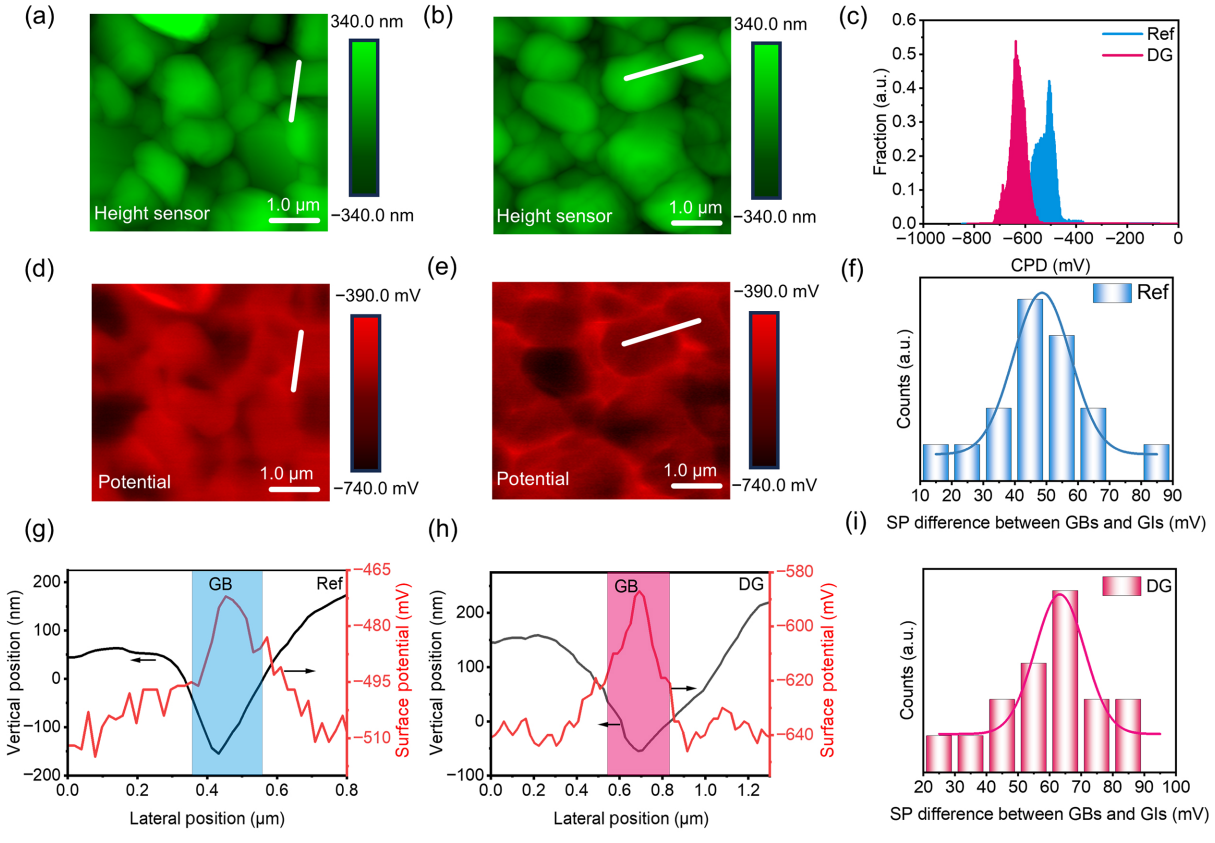

Figure 5 ((a) and (d)) Surface morphology. ((b) and (e)) KPFM data depicting potential maps for the Ref and DG absorber layers. ((c) and (f)) Grain boundaries are marked in the surface potential maps and corresponding potential curves. (g) Average contact potential difference. ((h) and (i)) Surface potential difference distributions at specified GB locations for the Ref and DG samples.

compared with the Ref sample (121 nm), providing a favorable template for uniform CdS buffer layer deposition. KPFM measurements (Figs. 5(b) and 5(e)) indicate that both samples display negative surface potentials (SP), associated with abundant negatively charged surface defects in CZTSSe. Notably, the DG sample presents a more negative SP, implying a lower electron affinity and higher work function [43], which aligns with UPS results. This shift originates primarily from the Ge substitution-induced bandgap widening. As shown in Fig. 5(g), the DG sample exhibits a more negative average contact potential difference (CPD) and a larger surface work function, which contribute to grain boundary (GB) passivation and improved charge transport and collection [44, 45]. Further analysis (Figs. 5(h) and 5(i)) reveals that GBs in both samples exhibit higher SP values than grain interiors (GIs), indicating downward band bending at GBs. This bending arises from S-rich CZTSSe promoting donor-type defects at GBs, attracting electrons and confining holes to suppress recombination. The enhanced GB-to-GI SP difference in DG strengthens band bending and hole barriers, facilitating carrier separation.

2.4 Device performance and efficiency enhancement mechanisms

To elucidate the optimization mechanism of the S/Ge dual gradient structure on the performance of CZTSSe solar cells, systematic analyses of photovoltaic characteristics and carrier dynamics were conducted. Figure 6(a) shows the device structure schematic. Statistical photovoltaic parameters are provided in Fig. S8 in the ESM and the optimal performance curves in Fig. 6(b). Notably, the DG device demonstrates satisfactory photovoltaic performance, offering a PCE of 9.36%, a V_{OC} of 0.46 V, a J_{SC} of 32.39 mA/cm^2, and a fill factor (FF) of 63.21%. In contrast, the reference device yields an unsatisfactory PCE of 7.43%, a V_{OC} of 0.39 V, a J_{SC} of 31.82 mA/cm^2, and an FF of 59.93%. This improvement in PCE for DG device primarily stems from the broadening of spectral response and optimization of carrier transport pathways achieved by the dual gradient structure. Specific parameters are detailed in Table 1.

DG device shows a more pronounced S-shaped bend at 0.2 V in the dark current density–voltage (J–V) curves (Fig. 6(c)), reflecting effective passivation of interfacial defects. Device characteristics were further quantified via J–V curves fitting (Fig. S9 in the ESM and Table 1), with calculation equation detailed in Note S3 in the ESM. The DG device shows a notable reduction in reverse saturation current density (J_0) from 5.13 × 10^{-3} to 7.18 × 10^{-4} mA/cm^2, a decrease in parallel conductance (G_R) from 4.15 to 2.33 mS/cm^2, the ideality factor (A_R) decreases from 1.89 to 1.76, and a lower series

Table 1 Photovoltaic-related parameters of the optimal Ref and DG devices

Devices	V_{OC} (V)	J_{SC} (mA/cm^2)	FF (%)	PCE (%)	E_g (eV)	E_u (meV)	A_R	J_0 (mA/cm^2)	R_S (Ω·cm^2)	G_R (mS/cm^2)
Ref	0.39	31.82	59.93	7.43	1.00	27.79	1.89	5.13 × 10^{-3}	0.78	4.15
DG	0.46	32.39	63.21	9.36	1.06	23.90	1.76	7.18 × 10^{-4}	0.46	2.33

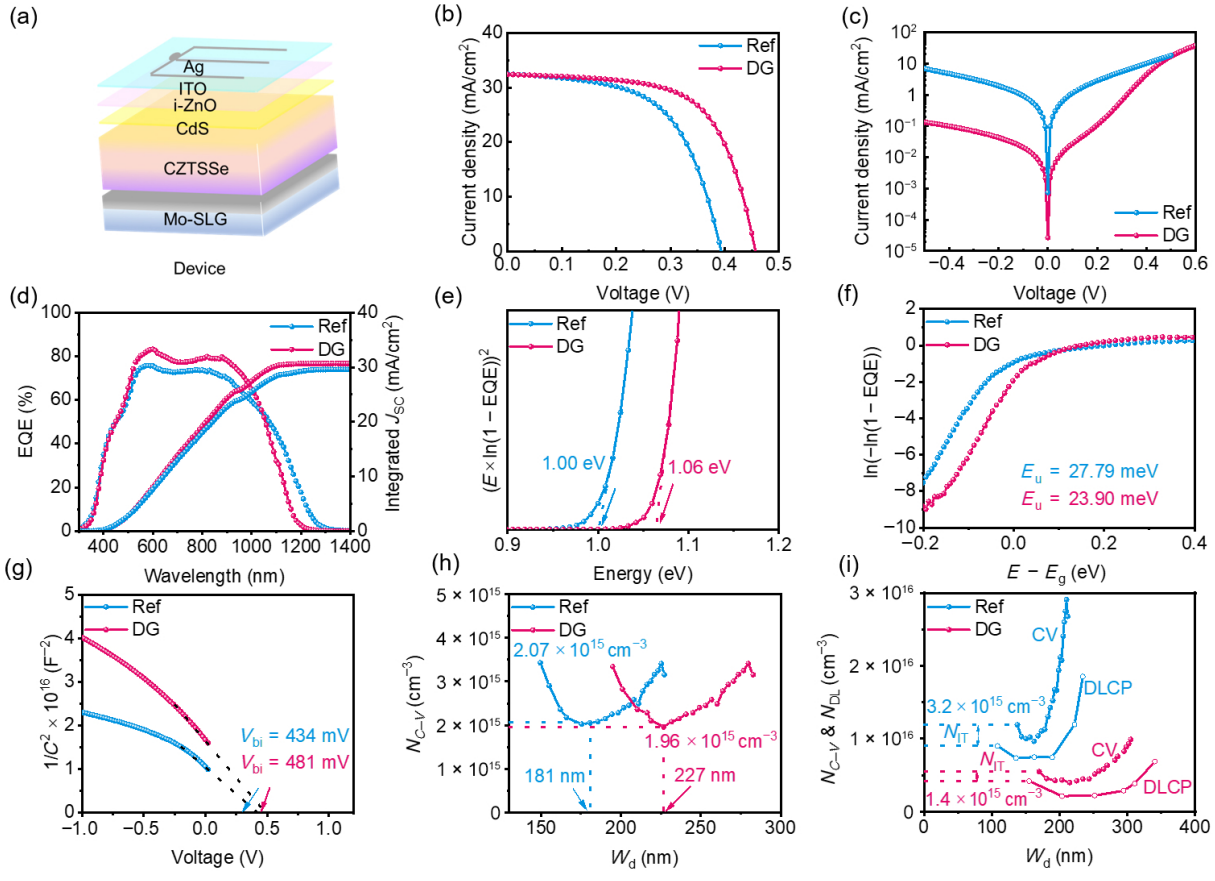

Figure 6 (a) Schematic diagram of the device structure. ((b) and (c)) *J*–*V* curves of the Ref and DG devices under illumination and in the dark. (d) EQE and J_{SC} curves for Ref and DG samples. (e) Band gaps fitted from EQE. (f) Fitted E_u. (g) $1/C^2$–*V* curves. (h) Calculated W_d and N_{C-V}. (i) *C*–*V* and DLCP curves.

resistance (R_S) from 0.78 to 0.46 Ω·cm². These parameter improvements collectively indicate that the DG device exhibits enhanced diode rectification behavior and improved carrier transport properties [46].

The external quantum efficiency (EQE) spectra (Fig. 6(d)) reveal a broad enhancement across the 500–1000 nm wavelength range in the DG device, attributed to improved absorber layer quality and CdS/CZTSSe interface quality. Conversely, the spectral response in the 1100–1300 nm range decreases, which results from the widened bandgap and correspondingly narrowed absorption edge induced by S/Ge incorporation [47]. Despite this bandgap increase, the DG device achieves a higher total integrated current, attributable to the effective suppression of Sn-related defects and band tail states. Figure 6(e) shows the bandgap values derived from EQE fitting. The band gap increases slightly from 1.00 eV (Ref) to 1.06 eV (DG), consistent with the bandgaps obtained by UPS. The Urbach energy (E_u) serves as a crucial indicator for the tail effect response and is one of the key factors influencing device performance [48]. Its value is primarily extracted from the inverse of the slope of the linear portion in the relationship plot between ln(−ln(1 − EQE)) and (E − E_g), where E represents the photon energy, as shown in Fig. 6(f). The E_u value of DG decreased to 23.90 meV relative to 27.79 meV (Ref), further confirming the significant reduction in band-tailed state density and the effective suppression of defect-induced non-radiative recombination [49, 50].

To investigate carrier transport behavior and defect state distribution in detail, we systematically characterized the devices using capacitance–voltage (*C*–*V*) profiling and drive-level capacitance profiling (DLCP) [51]. The *C*–*V* and extended $1/C^2$–*V* plots (Fig. S10 in the ESM and Figs. 6(g)–6(i)) allowed extraction of the depletion width (W_d), free carrier concentration (N_{C-V}), and built-in potential (V_{bi}) using the relationships summarized in Note S4 in the ESM, with numerical results listed in Table 2. As shown in Fig. 6(g), the V_{bi} values are determined from the extrapolated intercept of the linear region in the $1/C^2$–*V* plot with the voltage axis; the V_{bi} values for DG and Ref are 481 and 434 meV, respectively. The enhanced V_{bi} in DG directly strengthens the internal electric field at the CdS/CZTSSe heterojunction. This enhancement is closely related to the sulfur-rich gradient at the front interface, which provides a stronger driving force for carrier extraction and contributes to an improved V_{OC}. Figure 6(h) shows that W_d increases from 181 nm in Ref to 227 nm in DG, which helps suppress carrier recombination and associated V_{OC} loss. Meanwhile, the N_{C-V} of Ref is 2.07 × 10¹⁵ cm⁻³, while that of DG decreases to 1.96 × 10¹⁵ cm⁻³, a reduction attributed to the diminished density of [V_{Cu} + Zn_{Cu}] defect clusters and the suppression of Sn-related defects and secondary phases under dual-gradient modulation. Furthermore, the interfacial defect concentration (N_{IT}) was calculated using the equation $N_{IT} = N_{C-V} - N_{DL}$, where N_{DL} is defined as the carrier concentration measured by

Table 2 Relevant parameters from *C*–*V* and DLCP tests for Ref and DG devices

Devices	N_{C-V} (cm⁻³)	W_d (nm)	V_{bi} (mV)	N_{IT} (cm⁻³)
Ref	2.07 × 10¹⁵	181	434	3.2 × 10¹⁵
DG	1.96 × 10¹⁵	227	481	1.4 × 10¹⁵

DLCP (based on the relative content of N_{C-V} and N_{DL} at 0 V bias, Fig. 6(i)) [52]. The calculated N_{IT} decreases from 3.20 × 10^{15} and 1.40 × 10^{15} cm^{-3}, consistent with the observed reduction in E_u and the decreased defect state concentration measured in the space-limited current test (detailed calculations are presented in Fig. S11 and Note S5 in the ESM). These results demonstrate that the dual-gradient structure effectively suppresses defect states, optimizes the space-charge region, and reduces recombination losses.

Electrochemical impedance spectroscopy (EIS, Fig. S12 and Table S6 in the ESM) analysis further revealed that the junction resistance (R_j) of DG increased from 159 to 204 Ω, and the carrier lifetime extended from 1.75 to 2.20 μs (Note S6 in the ESM). This confirms that the dual gradient enhances charge collection efficiency by reconstructing carrier transport pathways and prolonging minority carrier diffusion lengths [53], providing kinetic support for the improvement in V_{OC} and FF. The S/Ge dual-gradient comprehensively enhances CZTSSe solar cell performance through synergistic effects of bandgap broadening, defect passivation, interface optimization, and carrier dynamics regulation, ultimately achieving a breakthrough in PCE from 7.43% to 9.36%.

3 Conclusions

In conclusion, this study addresses the technical bottleneck of precisely constructing CZTSSe dual-gradient structures by innovatively proposing a SnS-GeSe co-sulfoselenization strategy based on sequential reactions. Using a single heat treatment process, it successfully achieves spatial band engineering of the absorption layer, overcoming the complexity limitations of traditional stepwise doping techniques. During selenization, the Ge-Se liquid phase formed between GeSe and Se promotes Ge migration and enrichment toward the back interface, while S released from SnS accumulates at the front surface, forming an S-rich region, ultimately establishing a S/Ge dual gradient bandgap structure. In this process, the Sn_2Se_3 transition phase and Ge-Se liquid phase not only promote grain growth to enhance the quality of the absorber layer but also passivate defects, improve minority carrier lifetime, and reduce non-radiative recombination. These synergistic effects enable the device to achieve a PCE of 9.36% (with a 70 mV increase in V_{OC}), providing a novel pathway for the green and low-cost fabrication of kesterite solar cells.

Electronic Supplementary Material: Supplementary material (experimental procedures and characterization related to CZTSSe solar cells, SEM images, statistical results, *J*–*V* curves, device parameters list (Tables S2 and S3), device parameters by fitting dark state *J*–*V*, EIS and its parameters (Table S6)) is available in the online version of this article at https://doi.org/10.26599/NR.2026.94908520.

Data availability

All data needed to support the conclusions in the paper are presented in the manuscript and the Electronic Supplementary Material. Additional data related to this paper may be requested from the corresponding author upon request.

Acknowledgements

This work was supported by the Programs for the National Natural Science Foundation of China (No. 62374051), Henan Provincial Natural Science Foundation (Nos. 252300421860 and 252300421861), and China Postdoctoral Science Foundation, 78th Batch (No. 2025M780080).

Declaration of competing interest

All the contributing authors report no conflict of interests in this work.

Author contribution statement

Y. B. Z.: Writing – original draft, experimental data collection and processing. Q. L., W. C. T., Z. X. H., and S. F. G.: Data curation, formal analysis, visualization. X. S. L.: Methodology, validation, resources. J. L. L., K. C., and Z.-l. D.: Writing – review & editing, supervision, methodology, funding acquisition. All the authors have approved the final manuscript.

Use of AI statement

None.

References

[1] Hadke, S. S.; Su, Z. H.; Meng, Q. B.; Xin, H.; Wu, S. X.; Liang, G. X.; Shao, Z. P.; Wong, L. H. Understanding efficiency losses from radiative and nonradiative recombination in $Cu_2ZnSn(S,Se)_4$ solar cells. *Nat. Commun.* **2025**, *16*, 8240.

[2] Zhang, Y. H.; Siqin, L.; Liu, R. J.; Bai, Y. J.; Qiao, J. Q.; Yang, C. J.; Luan, H. M.; Cui, G. N.; Yang, Y. C.; Yao, B. et al. Boosting spectral response at band edge and charge transport in CZTSSe solar cells by periodic Mo back-contact texturing. *Appl. Phys. Lett.* **2025**, *127*, 133902.

[3] Green, M. A.; Dunlop, E. D.; Yoshita, M.; Kopidakis, N.; Bothe, K.; Siefer, G.; Hao, X. J.; Jiang, J. Y. Solar cell efficiency tables (Version 66). *Prog. Photovoltaics: Res. Appl.* **2025**, *33*, 795–810.

[4] Keller, J.; Kiselman, K.; Donzel-Gargand, O.; Martin, N. M.; Babucci, M.; Lundberg, O.; Wallin, E.; Stolt, L.; Edoff, M. High-concentration silver alloying and steep back-contact gallium grading enabling copper indium gallium selenide solar cell with 23.6% efficiency. *Nat. Energy* **2024**, *9*, 467–478.

[5] Kim, S.; Márquez, J. A.; Unold, T.; Walsh, A. Upper limit to the photovoltaic efficiency of imperfect crystals from first principles. *Energy Environ. Sci.* **2020**, *13*, 1481–1491.

[6] Chen, S. Y.; Walsh, A.; Gong, X. G.; Wei, S. H. Classification of lattice defects in the kesterite Cu_2ZnSnS_4 and $Cu_2ZnSnSe_4$ earth-abundant solar cell absorbers. *Adv. Mater.* **2013**, *25*, 1522–1539.

[7] Duan, B. W.; Shi, J. J.; Li, D. M.; Luo, Y. H.; Wu, H. J.; Meng, Q. B. Underlying mechanism of the efficiency loss in CZTSSe solar cells: Disorder and deep defects. *Sci. China Mater.* **2020**, *63*, 2371–2396.

[8] Cao, L.; Wang, L. J.; Zhou, Z. J.; Zhou, T. X.; Li, R.; Zhang, H.; Wang, Z. T.; Wu, S. X.; Najar, A.; Tian, Q. W. et al. Modifying surface termination by bidentate chelating strategy enables 13.77% efficient kesterite solar cells. *Adv. Mater.* **2024**, *36*, 2311918.

[9] Fan, Q. M.; Tian, Q. W.; Wang, H. L.; Zhao, F. M.; Kong, J.; Wu, S. X. Regulating the starting location of front-gradient enabled highly efficient $Cu(In,Ga)Se_2$ solar cells via a facile thiol-amine solution approach. *J. Mater. Chem. A* **2018**, *6*, 4095–4101.

[10] Li, J. J.; Huang, Y. C.; Huang, J. L.; Liang, G. X.; Zhang, Y. X.; Rey, G.; Guo, F.; Su, Z. H.; Zhu, H. B.; Cai, L. L. et al. Defect control for 12.5% efficiency $Cu_2ZnSnSe_4$ kesterite thin-film solar cells by engineering of local chemical environment. *Adv. Mater.* **2020**, *32*, 2005268.

[11] Li, J. Q.; Yuan, Z. K.; Chen, S. Y.; Gong, X. G.; Wei, S. H. Effective and noneffective recombination center defects in Cu_2ZnSnS_4:

Significant difference in carrier capture cross sections. *Chem. Mater.* **2019**, *31*, 826–833.

[12] Zhao, X. Y.; Li, J. R.; Hu, C. Y.; Qi, Y. F.; Zhou, Z. J.; Kou, D. X.; Zhou, W. H.; Yuan, S. J.; Wu, S. X. Revealing the role of hydrogen in highly efficient Ag-substituted CZTSSe photovoltaic devices: Photoelectric properties modulation and defect passivation. *Nano-Micro Lett.* **2025**, *17*, 84.

[13] Zhu, A. Y.; Ding, R. X.; Xu, H. T.; Tong, C. J.; McKenna, K. P. Cu–Zn cation disorder in kesterite $Cu_2ZnSn(S_x,Se_{1-x})_4$ solar cells. *ACS Energy Lett.* **2024**, *9*, 497–503.

[14] Zhang, Z. Q.; Qi, Y. L.; Zhao, W. Q.; Liu, J. L.; Liu, X. S.; Cheng, K.; Du, Z. L. Nanoscale sharp bandgap gradient for efficiency improvement of $Cu_2ZnSn(S,Se)_4$ thin film solar cells. *J. Alloys Compd.* **2022**, *910*, 164665.

[15] Zhao, Y. H.; Chen, S.; Ishaq, M.; Cathelinaud, M.; Yan, C.; Ma, H. L.; Fan, P.; Zhang, X. H.; Su, Z. H.; Liang, G. X. Controllable double gradient bandgap strategy enables high efficiency solution-processed kesterite solar cells. *Adv. Funct. Mater.* **2024**, *34*, 2311992.

[16] Li, M. G.; Ma, D.; Yao, B.; Li, Y. E.; Ding, Z. H.; Wang, C. K.; Luan, H. M.; Zhu, C. J. Mechanism of improvement of the power conversion efficiency of $Cu_2ZnSn(S,Se)_4$ solar cells through changing Ag and Cd co-doping form from uniform to non-uniform. *Chem. Eng. J.* **2025**, *515*, 163564.

[17] Fu, J. J.; Kou, D. X.; Zhou, W. H.; Zhou, Z. J.; Yuan, S. J.; Qi, Y. F.; Wu, S. X. Ag, Ge dual-gradient substitution for low-energy loss and high-efficiency kesterite solar cells. *J. Mater. Chem. A* **2020**, *8*, 22292–22301.

[18] Zhao, N.; Sui, Y.; Ma, M. L.; Wang, T. Y.; Miao, C.; Wang, Z. W.; Yang, L. L.; Wang, F. Y.; Yao, B. Optimized grain growth for efficient solution-processed bi-doped $Cu_2ZnSn(S,Se)_4$ thin film solar cells via spin-coated layers adjustment and two-step selenization. *Ceram. Int.* **2024**, *50*, 11085–11093.

[19] Yao, G.; Wu, Z. C.; Kou, D. X.; Kong, B. Y.; Wei, H.; Shao, Z. P.; Zhou, W. H.; Zhou, Z. J.; Yuan, S. J.; Qi, Y. F. et al. Phase evolution extension of $Cu_2ZnSn(S,Se)_4$ absorber boosting the efficiency of kesterite solar cells to 14.99%. *ACS Energy Lett.* **2025**, *10*, 2761–2769.

[20] Yu, Z. X.; Li, C. H.; Chen, S.; Zheng, Z. H.; Fan, P.; Li, Y. F.; Tan, M. L.; Yan, C.; Zhang, X. H.; Su, Z. H. et al. Unveiling the selenization reaction mechanisms in ambient air-processed highly efficient kesterite solar cells. *Adv. Energy Mater.* **2023**, *13*, 2300521.

[21] Xu, B.; Ma, C. H.; Lu, X. S.; Liu, Y. L.; Zhang, Q.; Chen, Y.; Yang, P. X.; Chu, J. H.; Sun, L. Beyond 10% efficient $Cu_2ZnSn(S,Se)_4$ solar cells: Effects of the introduction of SnS powder during selenization process. *Sol. Energy Mater. Sol. Cells* **2020**, *210*, 110522.

[22] Yang, K. J.; Son, D. H.; Sung, S. J.; Sim, J. H.; Kim, Y. I.; Park, S. N.; Jeon, D. H.; Kim, J.; Hwang, D. K.; Jeon, C. W. et al. A band-gap-graded CZTSSe solar cell with 12.3% efficiency. *J. Mater. Chem. A* **2016**, *4*, 10151–10158.

[23] Zhang, X.; Zhou, Z. J.; Cao, L.; Kou, D. X.; Yuan, S. J.; Zheng, Z.; Yang, G.; Tian, Q. W.; Wu, S. X.; Liu, S. Z. Suppressed interface defects by $GeSe_2$ post-deposition treatment enables high-efficiency kesterite solar cells. *Adv. Funct. Mater.* **2023**, *33*, 2211315.

[24] Liu, J. L.; Liu, Z. W.; Gao, K.; Cai, H.; Liu, Y. J.; Zhao, W. Q.; Liu, X. S.; Cheng, K.; Du, Z. L. Back shallow Ge gradient enhanced carrier separation for CZTSe solar cells through a coselenization process. *ACS Appl. Mater. Interfaces* **2021**, *13*, 56302–56308.

[25] Liu, S.; Liu, J. L.; Xue, Y.; Zhu, Z. Y.; Dai, Y.; Liu, X. S.; Cheng, K.; Du, Z. L. Dual-functional GeSe–Se coselenization enabling synergistic defect-interface engineering for high-efficiency electrodeposited flexible CZTSe solar cells. *Nano Lett.* **2025**, *25*, 13144–13152.

[26] Tao, S. Y.; Wang, H. P.; Jia, M. Y.; Han, J.; Wu, Z. H.; Zhou, J. H.; Baranova, M.; Zhu, H. W.; Zhao, M.; Zhuang, D. M. Ge-doped CZTSe solar cell efficiency beyond 14% by suppressing recombination. *Adv. Funct. Mater.* **2025**, *35*, 2423251.

[27] Sun, Y.; Lin, S. P.; Li, W.; Cheng, S. Q.; Zhang, Y. X.; Liu, Y. M.; Liu, W. Review on alkali element doping in $Cu(In,Ga)Se_2$ thin films and solar cells. *Engineering* **2017**, *3*, 452–459.

[28] Andrade-Arvizu, J.; Izquierdo-Roca, V.; Becerril-Romero, I.; Vidal-Fuentes, P.; Fonoll-Rubio, R.; Sánchez, Y.; Placidi, M.; Calvo-Barrio, L.; Vigil-Galán, O.; Saucedo, E. Is it possible to develop complex S–Se graded band gap profiles in kesterite-based solar cells. *ACS Appl. Mater. Interfaces* **2019**, *11*, 32945–32956.

[29] Shah, U. A.; Wang, A.; Irfan Ullah, M.; Ishaq, M.; Shah, I. A.; Zeng, Y. Y.; Abbasi, M. S.; Umair, M. A.; Farooq, U.; Liang, G. X. et al. A deep dive into Cu_2ZnSnS_4 (CZTS) solar cells: A review of exploring roadblocks, breakthroughs, and shaping the future. *Small* **2024**, *20*, 2310584.

[30] Wang, A.; He, M. R.; Green, M. A.; Sun, K. W.; Hao, X. J. A critical review on the progress of kesterite solar cells: Current strategies and insights. *Adv. Energy Mater.* **2023**, *13*, 2203046.

[31] Chen, S. Y.; Walsh, A.; Luo, Y.; Yang, J. H.; Gong, X. G.; Wei, S. H. Wurtzite-derived polytypes of kesterite and stannite quaternary chalcogenide semiconductors. *Phys. Rev. B* **2010**, *82*, 195203.

[32] Xue, D. J.; Liu, S.-C.; Dai, C. M.; Chen, S. Y.; He, C.; Zhao, L.; Hu, J. S.; Wan, L. J. GeSe thin-film solar cells fabricated by self-regulated rapid thermal sublimation. *J. Am. Chem. Soc.* **2017**, *139*, 958–965.

[33] Son, D. H.; Kim, Y. I.; Kim, S. H.; Nam, D.; Cheong, H.; Kang, J. K.; Yang, K. J.; Kim, D. H. Effects of S and Se contents on the physical and photovoltaic properties of $Cu_2ZnSn(S_x, Se_{1-x})_4$ thin films: Achieving a PCE of 9.47%. *J. Mater. Chem. A* **2019**, *7*, 22986–22995.

[34] Jian, Y.; Zhao, Y. G.; Zhao, J.; Chen, S.; Su, Z. H.; Ma, H. L.; Zhang, X. H.; Liang, G. X. Controllable SnS-vapor-assisted selenization to enhance carrier transport for highly efficient kesterite solar cells. *Adv. Energy Mater.* **2025**, *15*, e04071.

[35] Liang, G. X.; Li, Z. D.; Ishaq, M.; Zheng, Z. H.; Su, Z. H.; Ma, H. L.; Zhang, X. H.; Fan, P.; Chen, S. Charge separation enhancement enables record photocurrent density in $Cu_2ZnSn(S,Se)_4$ photocathodes for efficient solar hydrogen production. *Adv. Energy Mater.* **2023**, *13*, 2300215.

[36] Dimitrievska, M.; Fairbrother, A.; Saucedo, E.; Pérez-Rodríguez, A.; Izquierdo-Roca, V. Influence of compositionally induced defects on the vibrational properties of device grade $Cu_2ZnSnSe_4$ absorbers for kesterite based solar cells. *Appl. Phys. Lett.* **2015**, *106*, 073903.

[37] Ma, J. J.; Liu, R. J.; Sun, H. H.; Meng, X. Q.; Han, B. Y.; Wang, R. S.; Chi, D.; Wang, T.; Yao, B.; Song, Y. P. et al. Delafossite $CuAlO_2$ modification-induced synergistic passivation effects for heterojunction interface and absorber toward efficient kesterite solar cells. *Sol. RRL* **2024**, *8*, 2300828.

[38] Zhao, Y. H.; Chen, X. Y.; Chen, S.; Zheng, Z. H.; Su, Z. H.; Ma, H. L.; Zhang, X. H.; Liang, G. X. Energy band alignment and defect synergistic regulation enable air-solution-processed kesterite solar cells with the lowest V_{OC} deficit. *Adv. Mater.* **2025**, *37*, 2409327.

[39] Dimitrievska, M.; Fairbrother, A.; Pérez-Rodríguez, A.; Saucedo, E.; Izquierdo-Roca, V. Raman scattering crystalline assessment of polycrystalline Cu_2ZnSnS_4 thin films for sustainable photovoltaic technologies: Phonon confinement model. *Acta Mater.* **2014**, *70*, 272–280.

[40] Zhao, X. Y.; Kou, D. X.; Zhou, W. H.; Zhou, Z. J.; Meng, Y. N.; Meng, Q. B.; Zheng, Z.; Wu, S. X. Nanoscale electrical property enhancement through antimony incorporation to pave the way for the development of low-temperature processed $Cu_2ZnSn(S,Se)_4$ solar cells. *J. Mater. Chem. A* **2019**, *7*, 3135–3142.

[41] Scragg, J. J.; Ericson, T.; Kubart, T.; Edoff, M.; Platzer-Björkman, C. Chemical insights into the instability of Cu_2ZnSnS_4 films during annealing. *Chem. Mater.* **2011**, *23*, 4625–4633.

[42] Guo, R.; Li, X.; Jiang, Y. H.; Zhou, T. X.; Xia, Y. M.; Wang, P.; Liang, Y.; Sui, Y. R.; Yao, B.; Liu, Y. Regulating Sn_{Zn} defects and optimizing bandgap in the $Cu_2ZnSn(S,Se)_4$ absorption layer by Ge gradient doping for efficient kesterite solar cells. *Ceram. Int.* **2024**, *50*, 18329–18336.

[43] Zhang, Z. J.; Gao, Q.; Guo, J. J.; Zhang, Y. H.; Han, Y. C.; Ao, J. P.; Jeng, M. J.; Liu, F. F.; Liu, W.; Zhang, Y. Over 10% efficient pure CZTSe solar cell fabricated by electrodeposition with Ge doping. *Sol. RRL* **2020**, *4*, 2000059.

[44] Ren, D. L.; Fu, B. Y.; Xiong, J.; Wang, Y.; Zhu, B.; Chen, S.; Li, Z. Q.; Ma, H. L.; Zhang, X. H.; Pan, D. C. et al. PO_4^{3-} tetrahedron assisted chelate engineering for 10.67%-efficient antimony selenosulfide solar cells. *Adv. Mater.* **2025**, *37*, 2416885.

[45] Ji, Y. X.; Zhao, X. Y.; Pan, Y. N.; Su, Z. H.; Lin, J. H.; Akinoglu, E. M.; Xu, Y.; Zhang, H. Y.; Zhao, P. J.; Dong, Y. et al. CuSCN modified back contacts for high performance CZTSSe solar cells. *Adv. Funct. Mater.* **2023**, *33*, 2211421.

[46] Chi, J. J.; Wei, H.; Chu, L. L.; Han, L. T.; Liu, T.; Zhong, X. Y.; Kou, D. X.; Zhou, W. H.; Zhou, Z. J.; Yuan, S. J. et al. Phase evolution regulation of CZTSSe absorbers via a ZnO blocking layer enables 14.45% efficient kesterite solar cells with low V_{OC} deficit. *Energy Environ. Sci.* **2025**, *18*, 8366–8381.

[47] Yu, Z. X.; Li, S. R.; Li, C. H.; Huang, S. H.; Wang, Y. H.; Su, Z. H.; Liang, G. X.; Yan, C. Dominant defect and microstructure transformation engineering for highly efficient low-bandgap stannite solar cells. *Chem. Eng. J.* **2025**, *508*, 161030.

[48] Du, Y.; Wang, S.; Tian, Q.; Zhao, Y.; Chang, X.; Xiao, H.; Deng, Y.; Chen, S.; Wu, S.; Liu, S. Defect engineering in earth-abundant $Cu_2ZnSn(S,Se)_4$ photovoltaic materials via Ga^{3+}-doping for over 12% efficient solar cells. *Adv. Funct. Mater.* **2021**, *31*, 2010325.

[49] Liu, J. L.; Wu, X. Y.; Xue, Y.; Liu, S.; Zhu, Z. Y.; Liu, X. S.; Cheng, K.; Du, Z. L. Se as hetero-nucleation seeds reinforcing intermetallic diffusion for improved electrodeposition-processed CZTS solar cells. *Nano Energy* **2024**, *130*, 110183.

[50] Wang, M. Y.; Geng, H.; Zhu, J. C.; Cui, Y. B.; Zhao, S. H.; Fu, J. J.; Kou, D. X.; Sun, J.; Zhao, C. L.; Wu, S. X. et al. Hyperactive selenium source yields kesterite solar cells with 12.86% efficiency. *Adv. Funct. Mater.* **2023**, *33*, 2307389.

[51] Yu, Q.; Shi, J. J.; Zhang, P. P.; Guo, L. B.; Min, X.; Luo, Y. H.; Wu, H. J.; Li, D. M.; Meng, Q. B. Impressive self-healing phenomenon of $Cu_2ZnSn(S, Se)_4$ solar cells. *Chin. Phys. B* **2018**, *27*, 066108.

[52] Yang, C. J.; Siqin, L.; Wang, Y. T.; Li, Y. F.; Li, W. B.; Li, S. Y.; Liu, R. J.; Luan, H. M.; Zhu, C. J. SnS-induced element diffusion simultaneous optimization of interface and bulk defects in high-efficiency CZTSSe solar cells. *Chem. Eng. J.* **2025**, *503*, 158283.

[53] Wang, L. J.; Wu, Z. C.; Han, L. T.; Ban, J. T.; Shang, C. J.; Zhou, Z. J.; Yang, G.; Zhao, D. D.; Zheng, Z.; Wu, S. X. Temperature-modulated nucleation engineering enables uniform distribution of cations for efficient kesterite solar cells. *Adv. Funct. Mater.* **2025**, *35*, 2424870.